

# Sound-speed tomography using first-arrival transmission ultrasound for a ring array

Youli Quan<sup>\*a,b</sup> and Lianjie Huang<sup>b</sup>

<sup>a</sup> Department of Geophysics, Stanford University, Stanford, CA 94305-2215

<sup>b</sup> Mail Stop D443, Los Alamos National Laboratory, Los Alamos, NM 87545

## ABSTRACT

Sound-speed tomography images can be used for cancer detection and diagnosis. Tumors have generally higher sound speeds than the surrounding tissue. Quality and resolution of tomography images are primarily determined by the insonification/illumination aperture of ultrasound and the capability of the tomography method for accurately handling heterogeneous nature of the breast. We investigate the capability of an efficient time-of-flight tomography method using transmission ultrasound from a ring array for reconstructing sound-speed images of the breast. The method uses first-arrival times of transmitted ultrasonic signals emerging from non-beamforming ultrasound transducers located around a ring. It properly accounts for ray bending within the breast by solving the eikonal equation using a finite-difference scheme. We test and validate the time-of-flight transmission tomography method using synthetic data for numerical breast phantoms containing various objects. In our simulation, the objects are immersed in water within a ring array. Two-dimensional synthetic data are generated using a finite-difference scheme to solve acoustic-wave equation in heterogeneous media. We study the reconstruction accuracy of the tomography method for objects with different sizes and shapes as well as different perturbations from the surrounding medium. In addition, we also address some specific data processing issues related to the tomography. Our tomography results demonstrate that the first-arrival transmission tomography method can accurately reconstruct objects larger than approximately five wavelengths of the incident ultrasound using a ring array.

**Keywords:** First-arrival time, ring array, sound speed, time-of-flight, tomography, transmission ultrasound.

## 1. INTRODUCTION

Ring transducers have been used for whole-breast scanning.<sup>1-5</sup> Ultrasound data acquired with a ring transducer can be used for sound-speed tomography, attenuation tomography, diffraction tomography, and reflection imaging.<sup>1-8</sup> Earlier ring transducers employ a transmitter-receiver pair that is mechanically rotated to collect data at different angles. The data acquisition using this configuration is very slow and seems impractical for clinic applications. Recent development of ring transducer arrays allows much faster data acquisition.<sup>2-4</sup> A ring transducer array is usually composed of hundreds to thousands of transducer elements arranged along a ring. A typical diameter of a ring array is 20 cm. When one transducer in the array transmits, all transducers including the transmitter itself receive ultrasound transmission and scattering signals. Experimental results from phantoms and voluntary patients using the ring transducers are available from a number of research groups.<sup>1-6</sup> However, we still need to understand how accurate the transmission tomography can be using data acquired using ring arrays.

In this paper, we conduct a comprehensive study on the reconstruction capability of a time-of-flight transmission tomography method for a ring transducer array using computer-simulated data for different numerical breast phantoms. We use a finite-difference time-domain wave-equation scheme to simulate ultrasonic-wave propagation through computer-generated numerical breast phantoms within a ring array. We carry out the simulations using high-performance computers. Simulations of ultrasonic-wave propagation and scattering can be easily performed for a large number of well-controlled breast phantoms, and help understand the features of wavefields acquired by a ring transducer array. The simulation can also be used to study the accuracy of time-of-flight transmission tomography for different sizes and shapes of phantom breast tissues. We study the capability of a time-of-flight tomography method for

[\\*quany@pangea.stanford.edu](mailto:*quany@pangea.stanford.edu); phone (650) 724-7297

reconstructing objects scanned by a ring array. The method properly accounts for ray bending during tomography inversion by solving the eikonal equation using a finite-difference scheme. We also investigate the reconstruction accuracy of the tomography method for objects having different perturbations from the surrounding medium. In addition, we address some specific data processing issues related to time-of-flight tomography. In a companion paper,<sup>8</sup> we study the reflection imaging using our sound-speed reconstruction results to further improve image resolution.

## 2. ULTRASONIC WAVE SIMULATION FOR THE RING TRANSDUCER ARRAY

We use the finite-difference method<sup>9</sup> to simulate acoustic-wave propagation in different numerical breast phantoms. A ring array with 256 transducers used during simulations is shown in Fig. 1. Numerical breast phantoms are placed inside the ring transducer and immersed in water. The ultrasound source  $S(t)$  used in our simulations is

$$S(t) = [1 - 2(\pi f_o t)^2] \exp[-(\pi f_o t)^2], \quad (1)$$

where  $t$  is time and  $f_o$  is the central frequency of the source. When one transmitter transmits, all transducers simultaneously record ultrasound signals. We conduct 256 finite-difference simulations for each numerical phantom. If it takes half an hour to run the finite-difference program for a transmitter on one computer, it would take about a week to do a complete simulation for 256 transmitters, and would take months for tens of different numerical phantoms used to study the imaging capability using a ring array. These simulations require super-computing capabilities. We use computer clusters and a parallel finite-difference program for the simulations. Table 1 lists some of the modeling parameters used in the finite-difference simulations. Figure 2 is a typical simulated dataset recorded with the ring array. The direct wave is the main event seen in the data. Travel times (or time-of-flights) of the direct wave are picked and used for sound-speed tomography. The reflection or scattering waves in the data can be used for reflection image reconstruction studies.

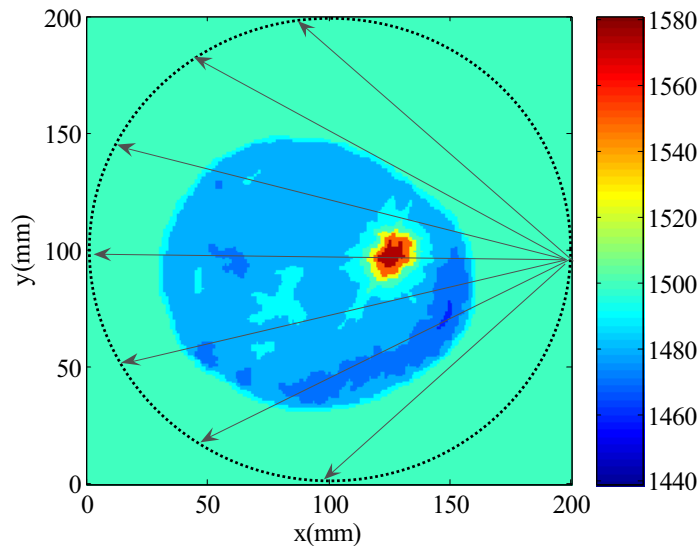


Figure 1. Illustration of a ring array and a numerical breast phantom immersed in water. Arrows depict ultrasonic-wave propagation from a transmitter. Color map shows the sound speed in m/sec.

Table 1. Parameters used in finite-difference simulations

Source central frequency ( $f_o$ )	0.5 MHz
Grid size of the model	0.1 mm
Time step	0.03 $\mu$ sec
Number of grids	2051 x 2051
Time signal length	150 $\mu$ sec

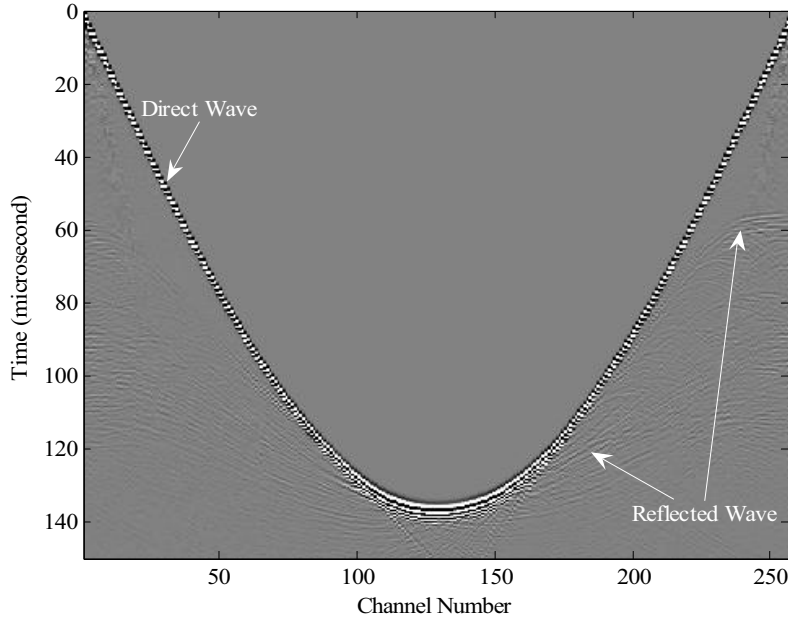


Figure 2. Simulated ring-array data using the numerical breast phantom shown in Fig. 1. The arrival time of the direct wave is used for sound-speed tomography and the reflected signals can be used for reflection image reconstruction.

### 3. DATA ANALYSIS AND TRAVEL-TIME PICKING

Before picking the travel-time of the direct wave for sound-speed tomography, let us take a closer look at the simulated data. Figure 3a shows a model that contains only a low sound-speed object within the ring array. We use this simple model to demonstrate some basic features of the ring array data. It can be seen from Fig. 3b that the forward scattering can cause interference with the direct wave. For this model, the scattering energy is weak because the impedance contrast between the circular object and water background is small. The scattering waves exhibit different patterns as the transmitter location changes. For a more realistic model, e.g., the one shown in Fig. 1, the reflection and scattering waves have much more complicated patterns as shown in Fig. 2.

The travel time of transmitted (or direct) wave is used to reconstruct the sound-speed distribution. We first generate a reference dataset using water-only as the model, and then pick the travel-time difference between reference data and study data. Figure 4 shows the comparison of reference data and study data shown in Fig. 3b. Figures 4a, b are signals within the interference zone. Their travel times, amplitudes and waveforms are different from those of the reference water data. We determine the travel-time difference ( $dT$ ) using two different methods: crosscorrelation and first-break picking. The absolute travel-time  $T$  of the data is then obtained using

$$T = L / C_{water} + dT, \quad (2)$$

where  $L$  is the distance between transmitter and receiver, and  $C_{water}$  is the sound speed of water. Figure 4c shows the signal recorded at a channel where there is no inference from the scattering.

Travel times picked using the two different methods are shown in Fig. 5. The crosscorrelation method needs to use a certain length of the signal for data processing. Therefore, the scattering interference contained in the later part of waveform may affect the correlation result. The influence is seen near channel 124 (see the blue arrow in Fig. 3 and Fig. 4b) where a small negative  $dT$  is detected. The circular object in Fig. 3 has a lower sound-speed than water, thus a positive  $dT$  is expected for all travel time picks. The first break picking exhibits less or no influence caused by the later scattering arrivals. For this reason, we use the first break picking to determine the travel times in this noise-free simulation study. For noisy experimental data, however, the correlation method should be more robust and practical.

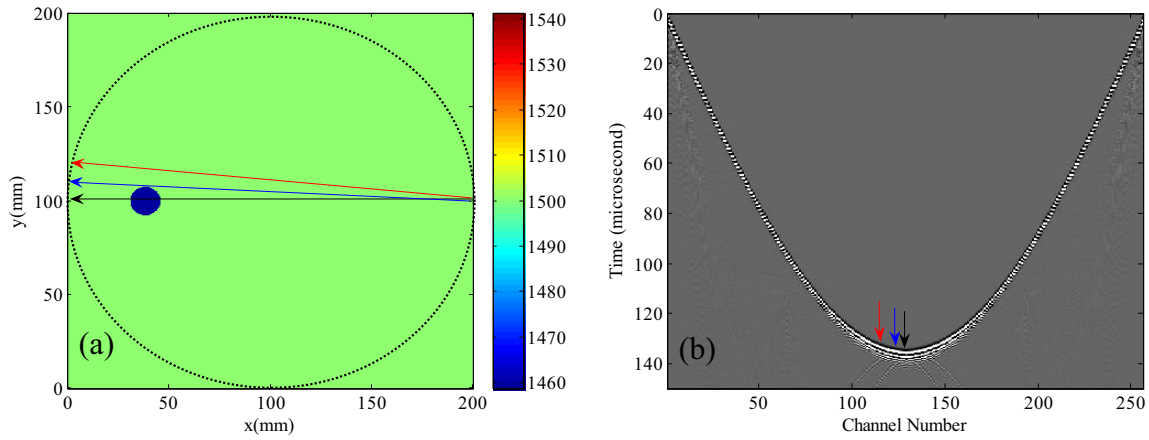


Figure 3. A simple numerical phantom with a low sound-speed object (a), and the corresponding ring transducer data for a transmitter (b). Three arrows with different colors indicate transducers and corresponding signals of interest, where ultrasonic wave passes through the object (black), passes the boundary (blue), and travels away from the object (red), respectively.

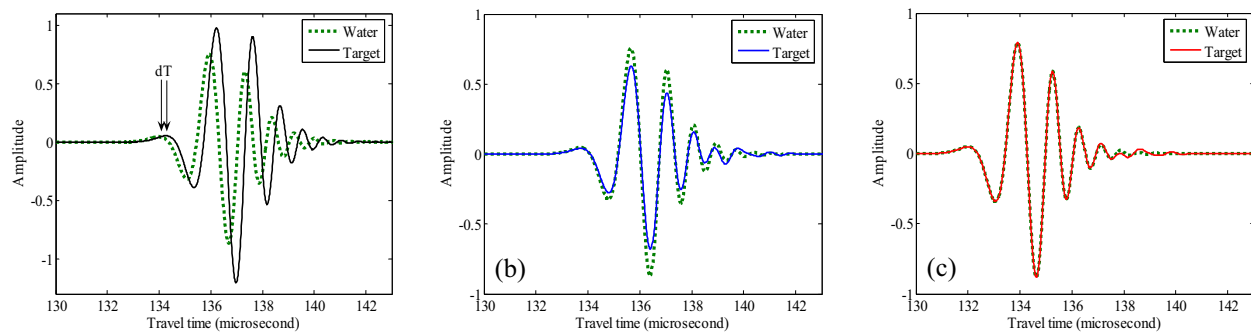


Figure 4. An overlay of the simulated data in Fig.3(b) and a reference data in water. Shown in (a), (b) and (c) are for the three different channels indicated in Fig. 3. The same color code as Fig.3 is used.

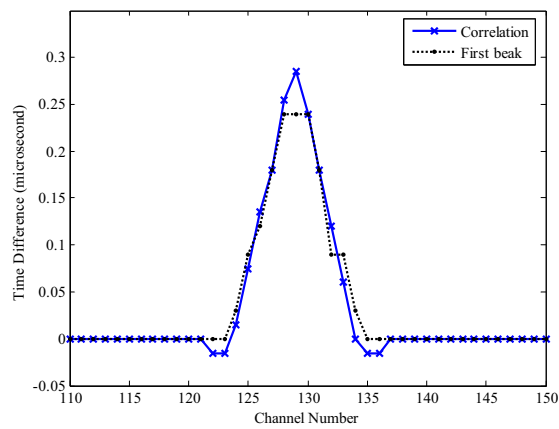


Figure 5. Comparison of travel times of the direct wave picked using the crosscorrelation and first break method for the data near those channels marked in Fig. 3.

## 4. TOMOGRAPHIC RECONSTRUCTION

### 4.1 Method

A regularized inversion method<sup>10</sup> is used to sound-speed reconstruction. Because the sound-speed distribution is not uniform, the ray (or beam) paths from transmitters to receivers are not straight lines. Therefore, we use bent rays in sound-speed reconstruction. First-arrival travel times and bent ray paths are calculated by solving the eikonal equation with a finite-difference method.<sup>11</sup> The reconstruction using bent rays is a nonlinear problem that can be solved iteratively. We start the iteration with a homogenous initial model that is divided into a uniform grid with  $M$  cells. The eikonal solver gives first-arrival travel times and ray paths for a given sound-speed model. Let  $\delta t_i$  be the travel-time difference between the observed time and the calculated time,  $l_j$  be the ray-path length in the  $j$ th cell, and  $\Delta s_j$  be the slowness perturbation of the  $j$ th cell. The slowness  $s$  is defined as the inverse of sound speed  $c$ , i.e.,  $s=1/c$ . For the  $i$ th ray path (or transmitter and receiver pair), we have a linear equation

$$\delta t_i = \sum_j^M l_{ij} \Delta s_j, \quad (3)$$

where  $i=1,2,\dots,N$ ;  $N$  is the total number of transmitter-receiver pairs to be used in reconstruction. Equation (3) can be written as a matrix form

$$\delta \mathbf{T} = \mathbf{L} \delta \mathbf{S}. \quad (4)$$

Solving equation (4) yields  $\Delta s_j$  from  $\delta \mathbf{T}$ , and generates an updated model by adding the perturbation  $\Delta s_j$  to the initial model. Travel times and ray paths are then recalculated using the updated model during next iteration. The iteration continues until the travel-time misfit  $\delta \mathbf{T}$  is not significantly improved from previous iteration. We reduce the roughness of the reconstructed model by applying regularization. Instead of solving equation (4), we actually solve a larger system of equations

$$\begin{bmatrix} \mathbf{C}_d^{-1/2} \delta \mathbf{T} \\ -\lambda \mathbf{C}_r \mathbf{S}_0 \end{bmatrix} = \begin{bmatrix} \mathbf{C}_d^{-1/2} \mathbf{L} \\ \lambda \mathbf{C}_r \end{bmatrix} \delta \mathbf{S}, \quad (5)$$

where  $\mathbf{C}_d$  is the data covariance matrix,  $\mathbf{C}_r$  is a roughing matrix,  $\lambda$  is a trade-off parameter,  $\mathbf{S}_0$  is the initial model of current iteration, and  $\delta \mathbf{S}$  is the model perturbation to be solved. The updated slowness model is obtained from  $\mathbf{S} = \mathbf{S}_0 + \delta \mathbf{S}$ . This system is solved by the LSQR method.<sup>12</sup>

### 4.2 Simple models

We first study reconstruction capability for simple objects. In Fig. 6, the objects with different sizes and shapes are located at the center of the ring. The central location should be favorable for the sound-speed reconstruction. Under this idealized condition, we investigate if we can reconstruct and resolve small objects. The two round objects have diameters of 15 mm and 5 mm, respectively, and the square one has a side of 13 mm. From the reconstruction images in Fig.6, we can see that the sound speeds of two larger objects are well reconstructed, and the smaller round object can be identified. Using our simulated data with a central frequency of 0.5 MHz and a wavelength of approximately 3 mm, we have difficulty to reconstruct the shape of the square and the absolute value of the sound speed of the smaller round object. Figure 7 gives another example the object that is located off the center. The sound-speed reconstruction is also accurate, though the difference shown in Fig. 7d seems larger than Fig. 6d.

We display the travel-time difference rather than the absolute time to visualize the travel-time picks. The time difference is obtained by subtracting the travel time of the water-only reference data, and displayed in a transmitter-receiver diagram. In Fig. 6b, the travel-time perturbation is a straight line, because the object is located at the center of the ring transducer. If the object is off the center, the travel-time perturbation exhibits a sine-shaped curve, as shown in Fig. 7b.

### 4.3 Numerical breast phantoms derived from *in-vitro* and *in-vivo* data

A ring transducer array has been used to collect data from phantoms and volunteers.<sup>5</sup> We use an *in-vitro* data for an experimental breast phantom and an *in-vivo* ultrasound breast data to reconstruct the sound-speed images, and use them

to derive two numerical breast phantoms shown in Figs. 8 and 10. The simulation study on these phantoms can in turn help understand the ring transducer data and interpreting the reconstruction results. Figure 8 shows the simulation for models derived from a phantom with four objects. One of the objects with an irregular shape is a tumor. We decompose the phantom into different parts and study the effects of each part. Row 1 in Fig. 8 is a homogenous round target. In Row 2, an irregular object with a higher sound speed is added. This higher sound-speed anomaly causes a lower travel-time perturbation (see the dark blue belt in Column b.) It can be seen from Column c that the anomalous sound-speed is reconstructed but not the shape. When a lower sound-speed object is added (see Row 3), a higher perturbation appears in the travel-time pick diagram (see the yellow belt in Column b.) Row 4 gives the simulation for a complete phantom. The main feature added here is a thin layer. Column c shows the reconstruction of this layer. Figure 9 is a detailed comparison between the actual sound-speed in Row 1 and its reconstruction through a cross line.

The numerical breast phantom in Fig. 1 (also shown in Fig. 10a) is derived from a sound-speed reconstruction result of the in-vivo data set mentioned above. The simulated ultrasonic data for a transmitter is shown in Fig.2. Figure 10 shows the phantom, travel-time picks, and our sound-speed reconstruction of the phantom. The reconstruction shows the most features in the phantom. Because the ray-based transmission tomography is a low-resolution technique, the reconstructed image in Fig. 10(c) looks like a smoother version of the numerical phantom depicted in Fig. 10(a).

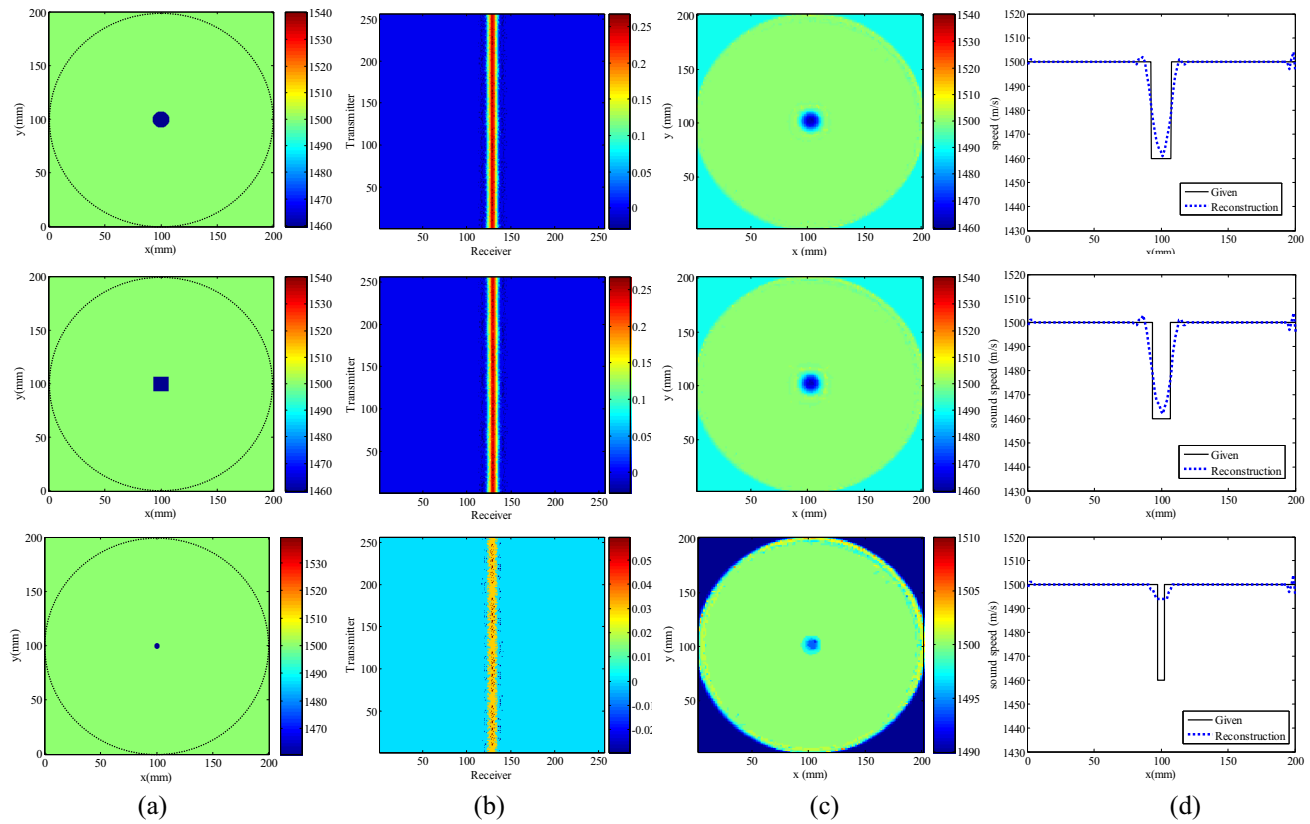


Figure 6. Numerical phantoms with an object at the center. (a) Given models. The color map is the sound speed (m/second). (b) The first-arrival travel time difference between water-only data and the study data; the unit of the color map is time (microsecond). (c) Reconstructed sound-speed images. (d) Comparison between the actual and reconstructed sound-speeds along a line across the center.

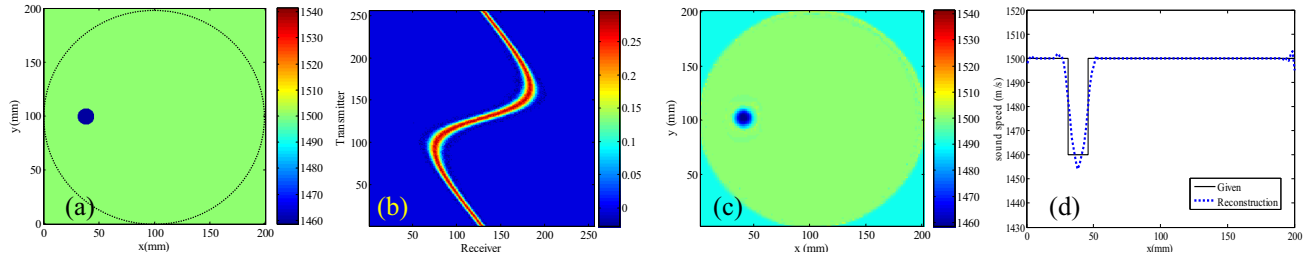


Figure 7. A numerical phantom with an object off the center. (a) The phantom. (b) Travel-time perturbation. (c) Reconstructed sound-speed. (d) A comparison between the actual and reconstructed sound-speeds.

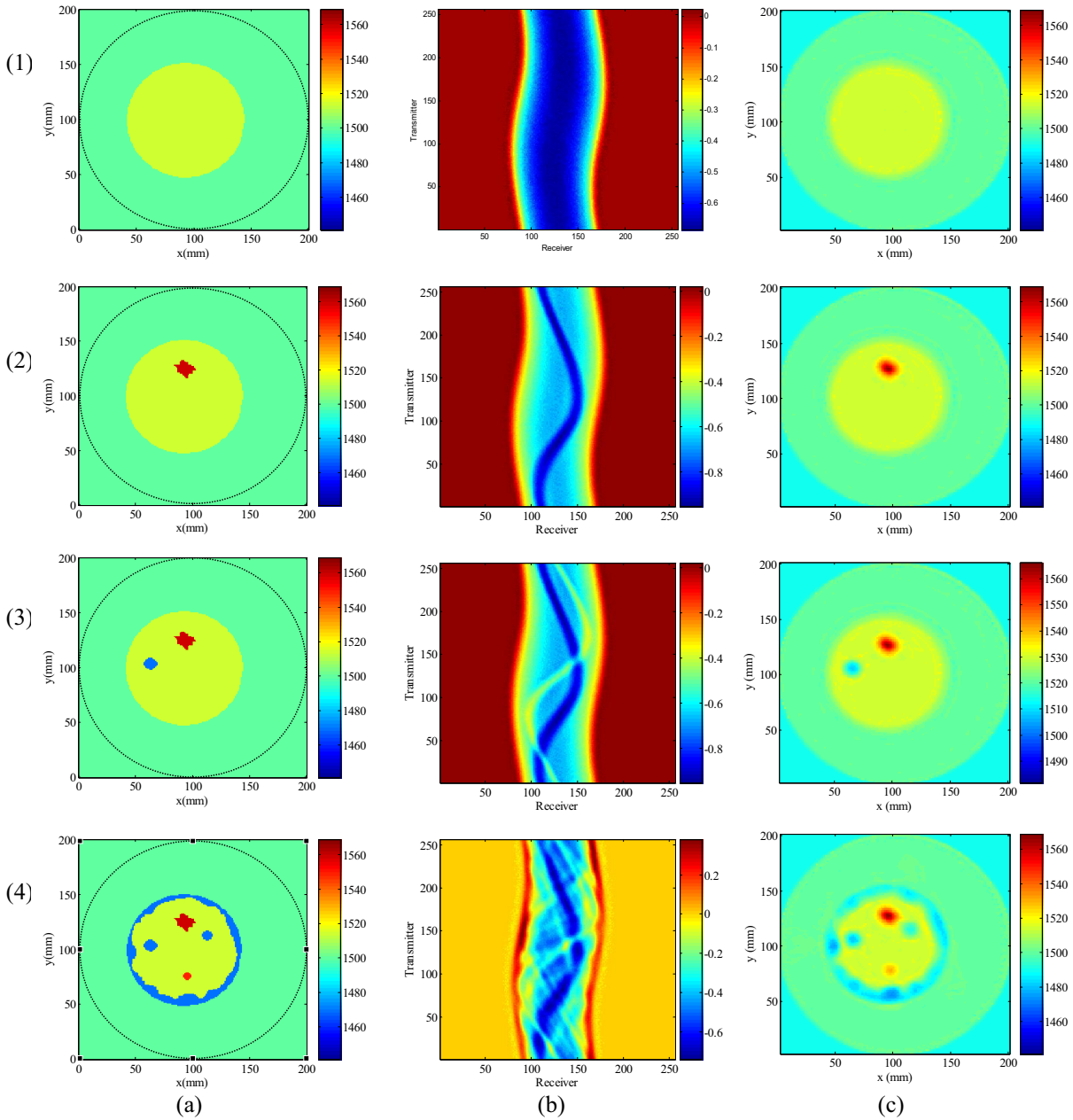


Figure 8. Simulation of a numerical phantom and its decomposition. Shown in (a) are the phantoms, those in (b) are travel-time perturbations, and the images (c) are reconstructed sound-speeds.

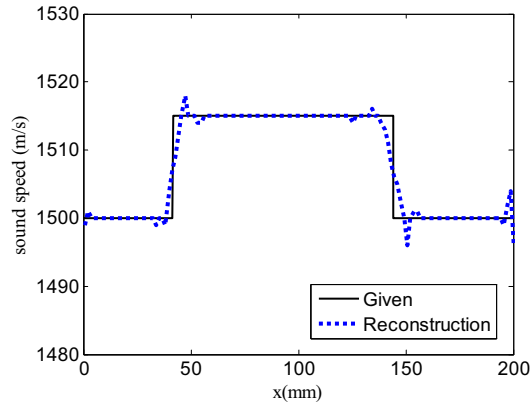


Figure 9. Cross-section comparison for the numerical phantoms shown in Row 1 in Fig. 8. The difference between the correct one and the reconstruction is invisible except at the edges.

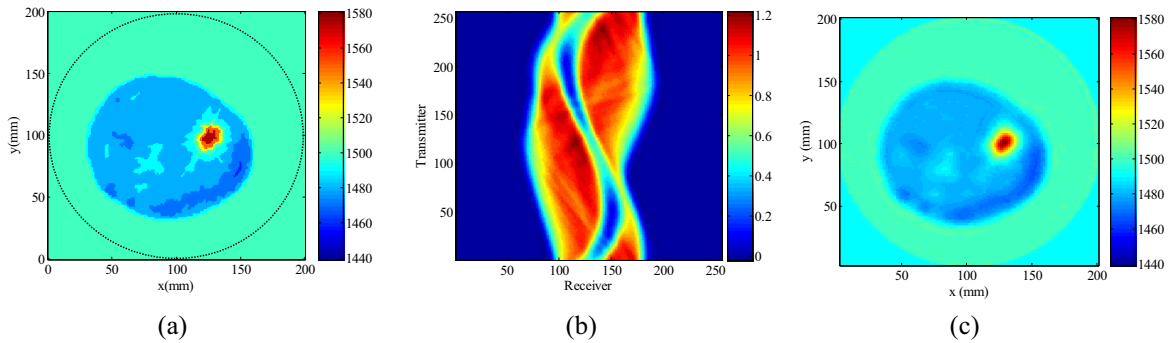


Figure 10. Sound-speed tomography for a numerical breast phantom derived from an *in-vivo* data collected using a ring array. (a) The numerical phantom. (b) The travel-time perturbation. (c) The reconstructed sound-speed image for the phantom.

## 5. CONCLUSIONS

The ring transducer array provides an ideal coverage for sound-speed transmission tomography. Our studies have demonstrated that the time-of-flight transmission tomography can accurately reconstruct the sound speed for an object larger than 5 wavelengths of the incident ultrasound. For objects with a size less than 2 wavelengths, the reconstruction may indicate the existence of the object, but does not recover the absolute value of the sound speed. The algorithms, e.g., the finite-difference eikonal solver for bent-ray computation and the linear system solver LSQR, used in our tomography reconstruction, are all computationally efficient. The computing time for a 5-iteration reconstruction was less than 3 minutes on a typical laptop computer, and was less than 1 minute on a state-of-the-art PC desktop.

## ACKNOWLEDGEMENTS

This work was supported through the U.S. DOE Laboratory-Directed Research and Development program at Los Alamos National Laboratory. The simulated data for the ring transducer array were computed using the computer clusters at Stanford Center for Computational Earth and Environmental Science (CEES). Numerical breast phantoms were derived from a breast phantom and an *in-vivo* breast tomography image provided by Karmanos Cancer Institute through Neb Duric. We thank Douglas Alde of Los Alamos National Laboratory for reviewing the paper.

## REFERENCES

1. J. S. Schreiman, J. Gisvold, J. F. Greenleaf and R. C. Bahn, "Ultrasound transmission computed tomography of the breast," *Radiology*, Vol. 150, 523–530, 1984.
2. R. C. Waag, and R. J. Fedewa, "A Ring Transducer System for Medical Ultrasound Research," *IEEE Transactions on Ultrasonics, Ferroelectrics, and Frequency Control*, Vol. 53, No 10, 1707–1718, 2006. □
3. M. P. Andre, H. S. Janee, P. J. Martin, G. P. Otto, B. A. Spivey, and D. A. Palmer, "High-speed data acquisition in a diffraction tomography system employing large-scale toroidal arrays," *Int. J. Imaging Syst. Technol.*, Vol. 8, 137–147, 1997.
4. R. Stotzka, J. Wurfel, T. O. Muller and H. Gemmeke, "Medical Imaging by Ultrasound–Computertomography ,": *Proc. SPIE Medical Imaging*, Vol. 4687, 11–119, 2002.
5. N. Duric, P. Littrup, L. Poulou, A. Babkin, R. Pevzner, E. Holsapple, and O. Rama, "Detection of breast cancer with ultrasound tomography: First results with the computerized ultrasound risk evaluation (C.U.R.E) prototype," *Medical Physics*, 2007. (Accepted)
6. L. Huang, N. Duric, and P. Littrup, "Ultrasonic breast imaging using a wave-equation migration method," *Proc. SPIE Medical Imaging* 5035, pp. 432–439, 2003.
7. L. Huang, N. Duric, and P. Littrup, "Breast imaging with time-reversed ultrasound", *Proc. SPIE Medical Imaging* 6147, pp156-167, 2006.
8. L. Huang and Y. Quan, "Ultrasound pulse-echo imaging using the split-step Fourier propagator," *Proc. SPIE Medical Imaging* 6513, 2007.
9. C. Wu and J. M. Harris, "An optimized variable-grid finite-difference method for seismic forward modeling," *Journal of Seismic Exploration*, Vol. 12, 343–353, 2004.
10. C. A. Zelt and P. J. Barton, "Three-dimensional seismic refraction tomography: A comparison of two methods applied to data from the Faeroe Basin," *J. Geophys. Res.*, Vol. 103, 7187–7210, 1998.
11. J. E. Vidale,, "Finite-difference calculation of traveltimes in three dimensions," *Geophysics*, Vol. 55, 521–526, 1990.
12. C. C. Paige and M. A. Saunders, "LSQR: An algorithm for sparse linear equations and sparse least squares," *Trans. Math Software*, Vol. 8, No 1, 43-71, 1982.